GEOPHYSICS, VOL. 50, NO. 8 (AUGUST 1985); P. 1266–1272, 8 FIGS.

Applications of elastic forward modeling to seismic interpretation

Moshe Reshef* and Dan Kosloff*

ABSTRACT

In the correct processing and interpretation of time sections gathered over complicated heterogeneous structures, acoustic assumptions no longer suffice and elastic effects need to be taken into consideration. This study presents numerical modeling results obtained with the Fourier method. Two classes of important geophysical problems were considered. The first class of problem was wave propagation in structures with both vertical and horizontal heterogeneities. Results of the calculations showed strong generation of converted phases and head waves. Generation of these phases is strongly dependent upon the velocity contrasts in the medium. The second class of problem was wave propagation in structures which contain both fluids and solids. The time sections recorded in the fluid regions again showed strong converted phases which could easily be misinterpreted as genuine acoustic reflections. The numerical results for the fluid-solid model proved to be in agreement with physical model results.

The presence of many phases on the time sections and snapshots requires that the elastic modeling method give accurate amplitudes and distinguish between *P*-waves and *S*-waves since otherwise their interpretation can become prohibitively complicated. In this respect, the Fourier method appears suitable because of its high accuracy and its ability to distinguish between *P*- and *S*-waves through respectively applying the numerical divergence and curl.

INTRODUCTION

Forward modeling has become a useful tool for interpretation in exploration geophysics. By modeling, field surveys can be simulated numerically, and computed results can be compared to field data.

Forward modeling gained additional importance with the recent trend to extract more information from seismic surveys by using amplitude values instead of only traveltimes, and with the use of shear wave information. Modeling is often used to simulate surveys in geologic areas with strong lateral velocity gradients. All these factors pose stringent requirements on the forward modeling algorithm, especially for elastic modeling. In evaluating various elastic forward modeling algorithms, it becomes clear that analytical methods are too restricted for simple geometries to be effective in general. Conversely, approximate methods like ray tracing do not always produce accurate results especially in problems with complicated geometries and rapid velocity variation. Ray tracing can also become prohibitively complicated for structures with many internal material interfaces. Therefore ray tracing can be useful for obtaining rapid approximate results, but it should not be used for accurate evaluations.

The class of modeling schemes which possess the desired accuracy for elastic problems includes direct methods like finite-differences, finite-elements, and the Fourier method. In this type of modeling the equations of motion are solved directly through a spatial and temporal discretization. These methods allow complete material variability and have no fundamental accuracy limitations. Their main drawback is their high cost.

In this study we present results obtained with a Fourier method modeling scheme for two-dimensional (2-D) heterogeneous elastic regions. A detailed description of the numerical algorithm is given in Kosloff et al. (1984).

We briefly describe the numerical scheme and show examples of its application to two important topics: first, a detailed study of elastic phenomena near complicated structures, and second, a calculation of synthetic time sections for a structure consisting of a fluid overlying layered solids.

BASIC EQUATIONS

In a 2-D continuous medium, the linearized equations of momentum conservation are given by

$$\rho f_x + \frac{\partial \sigma_{xx}}{\partial x} + \frac{\partial \sigma_{xy}}{\partial y} = \rho \ddot{U}_x,$$

Manuscript received by the Editor April 3, 1984; revised manuscript received January 31, 1985.
*Department of Geophysics, Tel Aviv University, Tel Aviv, Israel 69978; and Seismic Acoustics Laboratory, University of Houston, Houston, TX 77004.

and (1)

$$\rho f_y + \frac{\partial \sigma_{xy}}{\partial x} + \frac{\partial \sigma_{yy}}{\partial y} = \rho \ddot{U}_y,$$

where x and y are Cartesian coordinates, σ_{xx}, σ_{yy}, and σ_{xy} are the three stress components, U_x and U_y represent the displacements, f_x and f_y represent the body forces, and $\rho(x, y)$ is the density. In equation (1), as in the remainder of this work, a dot above a variable represents a time derivative.

Under infinitesimal deformation, the relations between the twice-differentiated time strain and displacement are given by

$$\ddot{e}_{xx} = \frac{\partial \ddot{U}_x}{\partial x},$$

$$\ddot{e}_{yy} = \frac{\partial \ddot{U}_y}{\partial y}, \quad (2)$$

and

$$\ddot{e}_{xy} = \frac{1}{2}\left(\frac{\partial \ddot{U}_x}{\partial y} + \frac{\partial \ddot{U}_y}{\partial x}\right)$$

where e_{xx}, e_{yy}, and e_{xy} represent the strain components.

After the substitution of equation (1) into equation (2), an alternative statement of momentum conservation is obtained:

$$\frac{\partial f_x}{\partial x} + \frac{\partial}{\partial x}\left[\frac{1}{\rho}\left(\frac{\partial \sigma_{xx}}{\partial x} + \frac{\partial \sigma_{xy}}{\partial y}\right)\right] = \ddot{e}_{xx},$$

$$\frac{\partial f_y}{\partial y} + \frac{\partial}{\partial y}\left[\frac{1}{\rho}\left(\frac{\partial \sigma_{xy}}{\partial x} + \frac{\partial \sigma_{yy}}{\partial y}\right)\right] = \ddot{e}_{yy},$$

and (3)

$$\frac{\partial f_x}{\partial y} + \frac{\partial f_y}{\partial x} + \frac{\partial}{\partial x}\left[\frac{1}{\rho}\left(\frac{\partial \sigma_{xx}}{\partial x} + \frac{\partial \sigma_{xy}}{\partial y}\right)\right] + \frac{\partial}{\partial y}\left[\frac{1}{\rho}\left(\frac{\partial \sigma_{xy}}{\partial x} + \frac{\partial \sigma_{yy}}{\partial y}\right)\right] = 2\ddot{e}_{xy}.$$

Equation (3) contains the stresses and strains as unknowns, whereas the displacements have been eliminated. In deriving this equation, no assumptions on material rheology are used and the equation also can be used for calculations for nonelastic media.

The three additional equations required for determining stresses and strains in the medium are supplied by the stress-strain relation. In the simplest case of an elastic and isotropic medium, these relations are given by

$$\sigma_{xx} = (\lambda + 2\mu)e_{xx} + e_{yy},$$

$$\sigma_{yy} = \lambda e_{xx} + (\lambda + 2\mu)e_{yy}, \quad (4)$$

and

$$\sigma_{xy} = 2\mu e_{xy}.$$

in which λ and μ represent the Lamé constant and the shear modulus, respectively.

To solve equations (3) and (4) for the three stresses, we use second-order differencing to advance in time. The spatial derivations are calculated with the Fourier method. The geology of the modeled region is represented through the material parameters λ, μ, and ρ. Initiation of the forward modeling is done through the force terms, with the option to use a pressure source, a shear source, or a directional force (Kosloff et al., 1984). Fourier method modeling allows a wide variety of output displays which facilitate interpretation of the results. These include snapshots of the stress components at fixed times, and displacement time histories at selected points from which synthetic time sections can be made. In addition, snapshots of the pressure field and the curl of the acceleration field can be produced. These show only P-waves and S-waves, respectively, and therefore are very useful for the isolation and interpretation of events.

EXAMPLES: WAVE PROPAGATION THROUGH LATERALLY HETEROGENEOUS STRUCTURES

Now we test the numerical modeling in two problems of wave propagation through laterally heterogeneous structures. In the first problem a localized source is excited above a corner boundary separating two homogeneous elastic regions with differing seismic velocities. The second case is wave propagation across an inclined fault structure.

Corner structure

This example considers wave propagation in a region consisting of two materials with differing velocities separated by a corner boundary (Figure 1).

We first consider motion after application of a pressure source at point S which lies in a low velocity region. The parameters for the problem were $V_{p1} = 2\ 700$ m/s, $V_{s1} = 1\ 500$ m/s, $V_{p2} = 4\ 000$ m/s and $V_{s2} = 2\ 200$ m/s. The calculation in this problem, and also in all the other examples of this section, used a grid size of 256×256 with spacing $DX = DY = 20$ m. The source wavelet had a Gaussian time dependence with a high-cut frequency of 35 Hz.

Snapshots of the P and S wavefronts (pressure and curl, respectively) at a specified time after the excitation of the source, are shown in Figures 1a and 1b. The P-wave snapshot (Figure 1a) is easier to interpret. In this figure, the primary P-wave is indicated by A whereas the reflected P-wave is indicated by B. The transmitted P-wave D has a wider wavefront due to the high velocity in the lower left region. There is also a distinct head wave C which connects the reflected and the transmitted P-waves.

The converted S-waves are shown in Figure 1b. We notice the asymmetry around the 45 degree axis passing through the corner and the source location. This figure is slightly more noisy than the previous one because of the extra derivative operation required to calculate the S-wave field (see Kosloff et al., 1984). The reflected and transmitted S-waves are indicated by A and C, respectively. In addition, four types of head waves can be seen in this example: event B which connects the reflected and transmitted S-waves, event G which connects the reflected S-wave and the transmitted P-wave, event D which connects the reflected S-wave and the reflected P-wave, and event F which connects the transmitted S-wave with the reflected P-wave.

When the velocities in the corner structure are interchanged, a totally different picture results. In the P-wave snapshot (Figure 2a) we can distinguish the initial P-wave A, the reflected P-wave B, the diffracted P-wave C which travels at the slower velocity V_{p2}, and a strong head wave D generated from a diffraction from the corner. The S-wave snapshot (Figure 2b) shows the reflected S-wave A, the weak diffracted

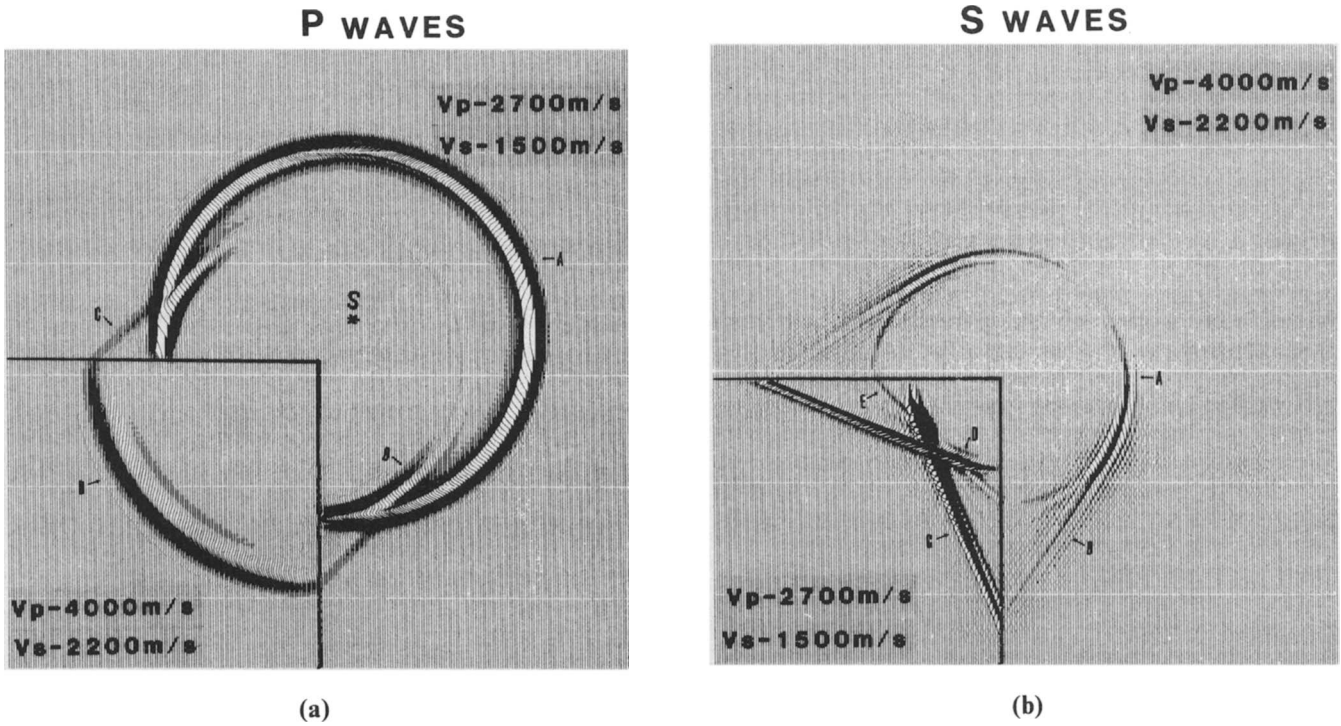

FIG. 1. (a) *P*-wave snapshot for the corner problem (high velocity inside the corner). (b) *S*-wave snapshot for the corner problem (high velocity inside the corner).

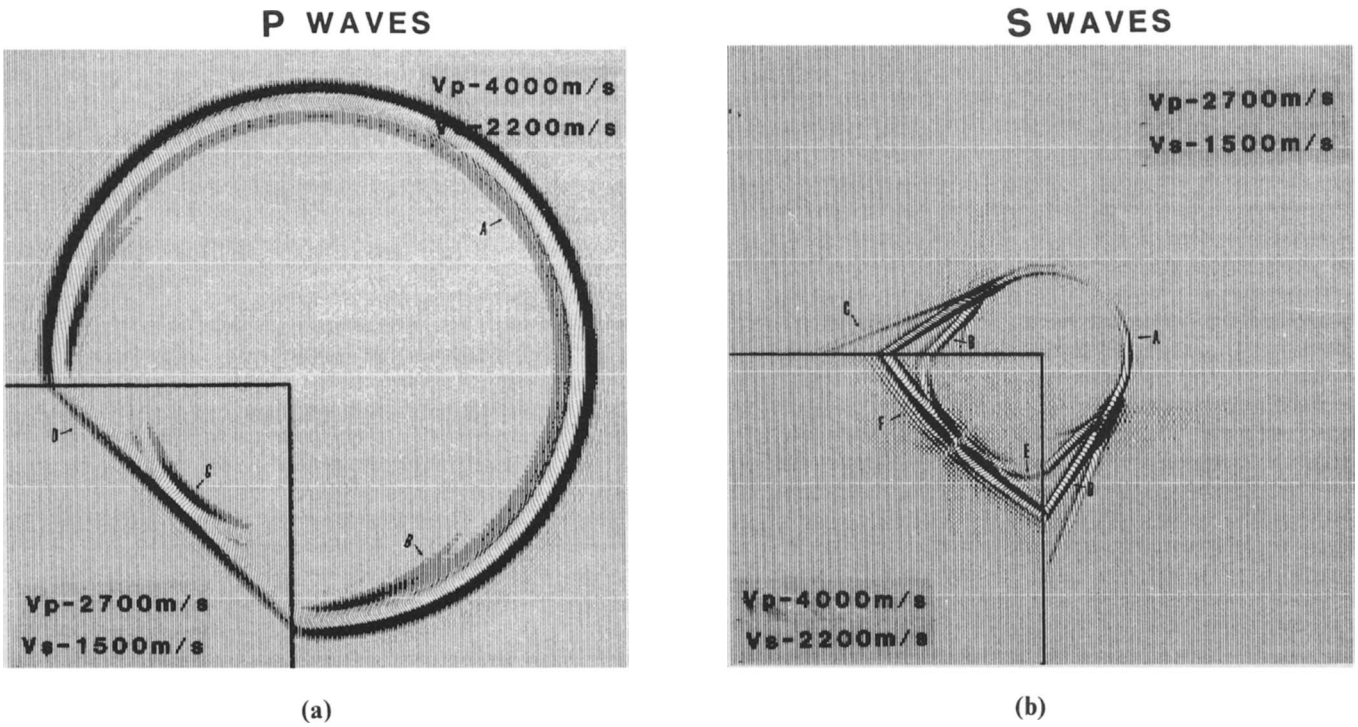

FIG. 2. (a) *P*-wave snapshot for the corner problem (low velocity inside the corner). (b) *S*-wave snapshot for the corner problem (low velocity inside the corner).

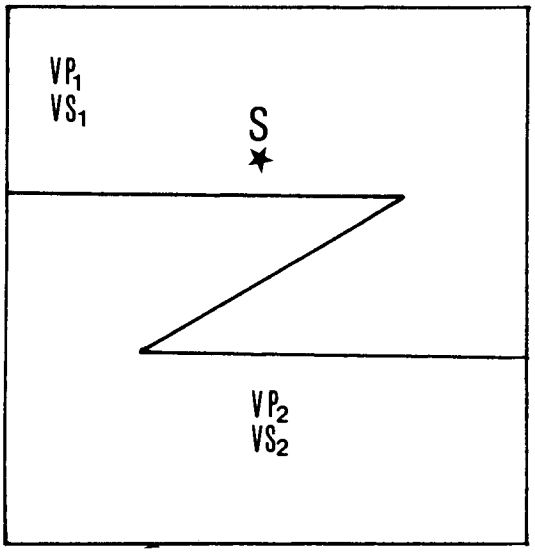

FIG. 3. Z type structure configuration.

S-wave D as well as three head waves B which connect the reflected P-wave with the reflected S-wave E, which connects the diffracted and reflected S-waves, and the very strong connecting head wave between the reflected P-wave and the diffracted S-wave (event C).

"Z" type structure

In this example we study wave propagation near an idealized overthrust structure. Figure 3 shows the structure in which S indicates the location of a pressure source with a high-cut frequency of 40 Hz. The P-wave velocities were 3 000 and 4 000 m/s for V_{p1} and V_{p2}, respectively, and the S-wave velocities were 1 700 and 2 400 m/s for V_{s1} and V_{s2}. The grid size used was 256 × 256 with a spacing of $DX = DY = 20$ m.

Snapshots of P and S wavefronts at a given time are shown in Figures 4a and 4b. Several events can be followed in the P-wave snapshot (Figure 4a), for example, the initial P-wave A, the reflection from the upper boundary B, the transmitted P-wave with the wider wavefront C, etc. Note the absorbing

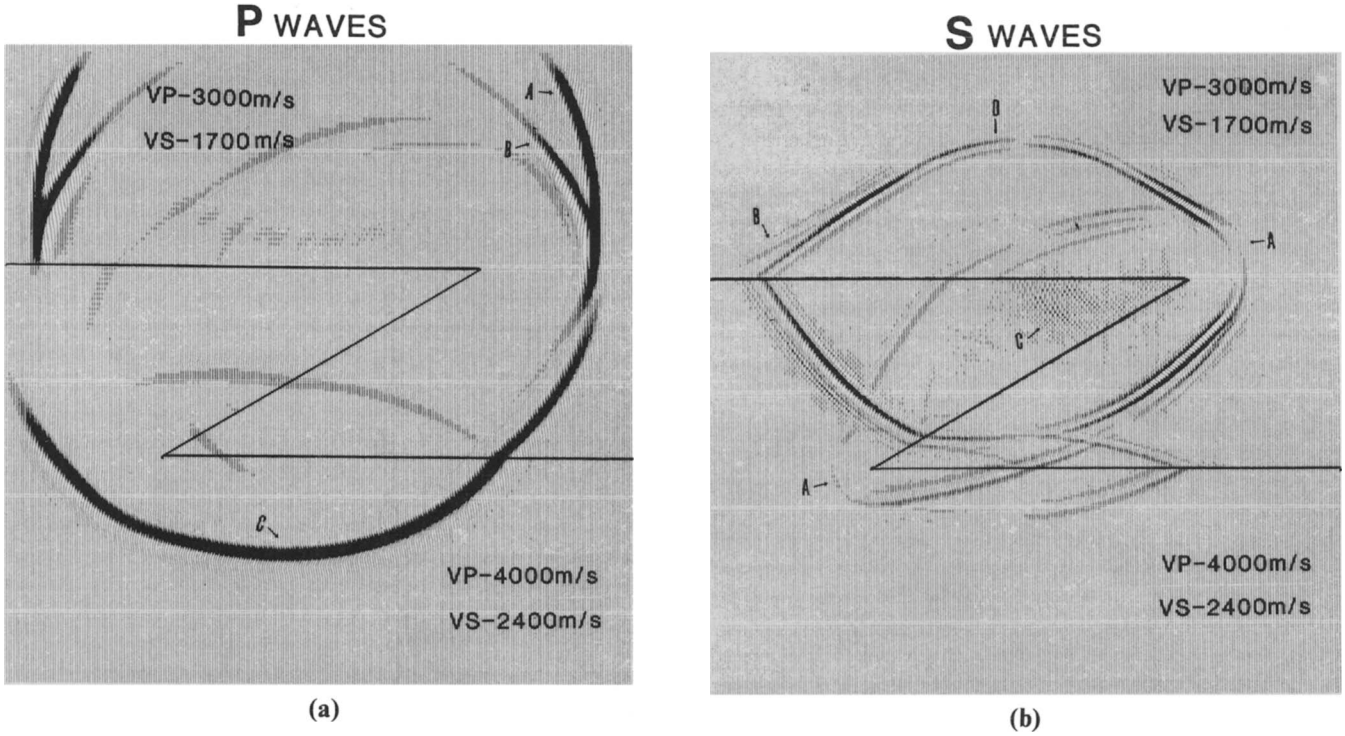

FIG. 4. (a) P-wave snapshot for the Z type structure. (b) S-wave snapshot for the Z type structure.

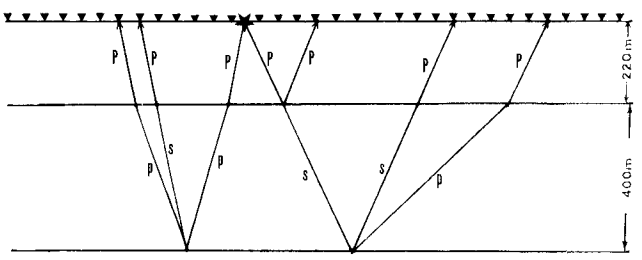

FIG. 5. Configuration and major raypaths of the fluid-solid problem.

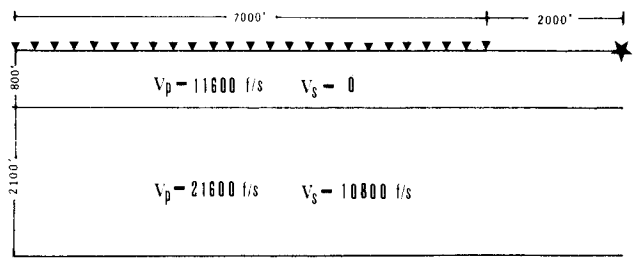

FIG. 7. Configuration of the tank model.

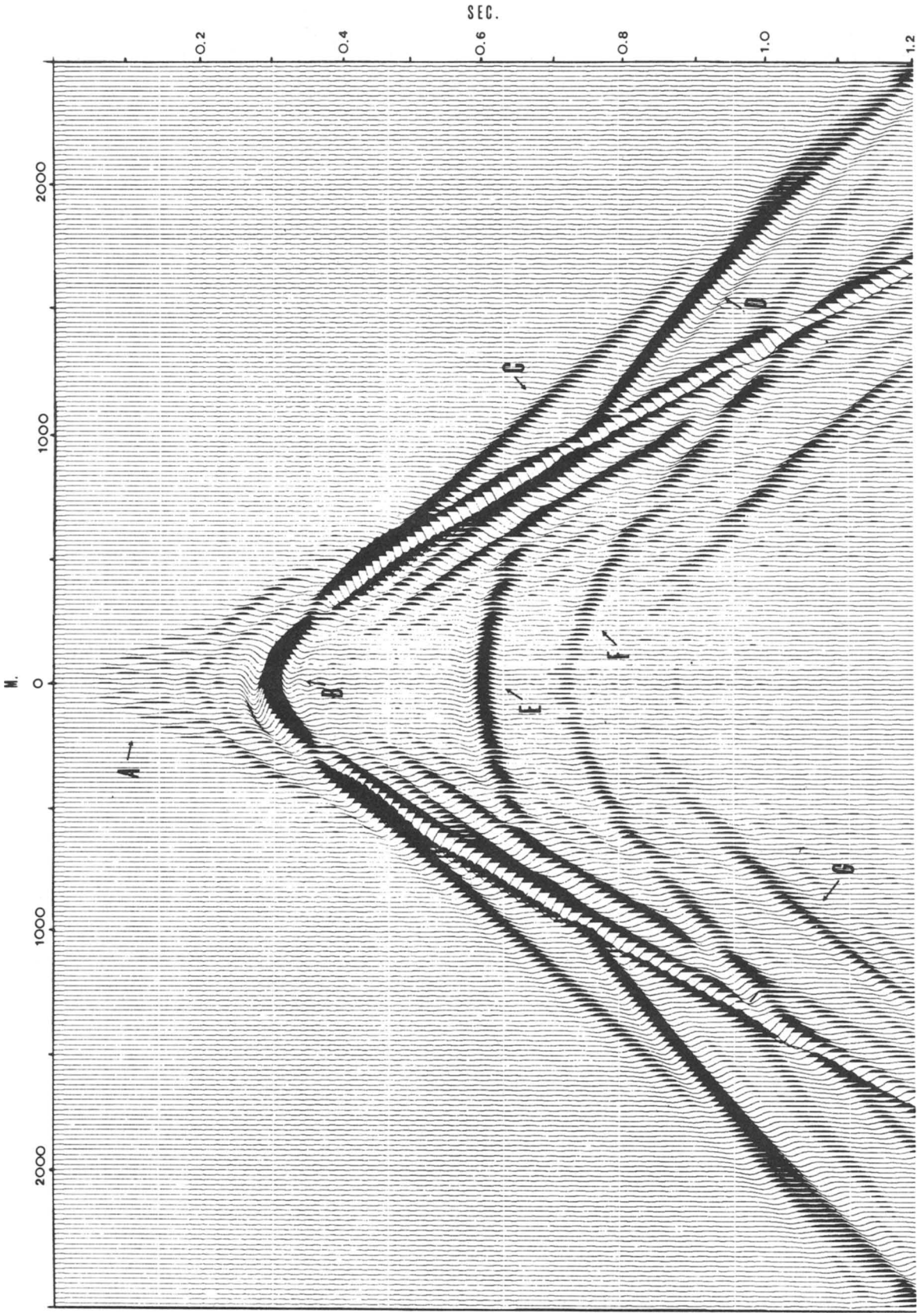

FIG. 6. Synthetic time section of the fluid-solid problem.

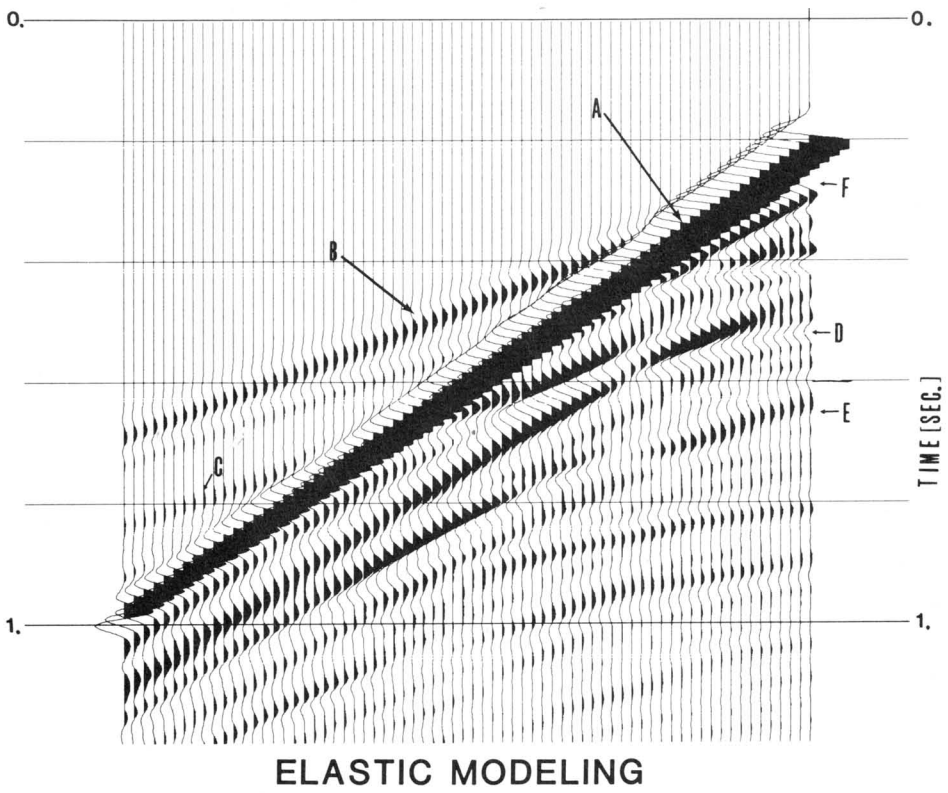

(a)

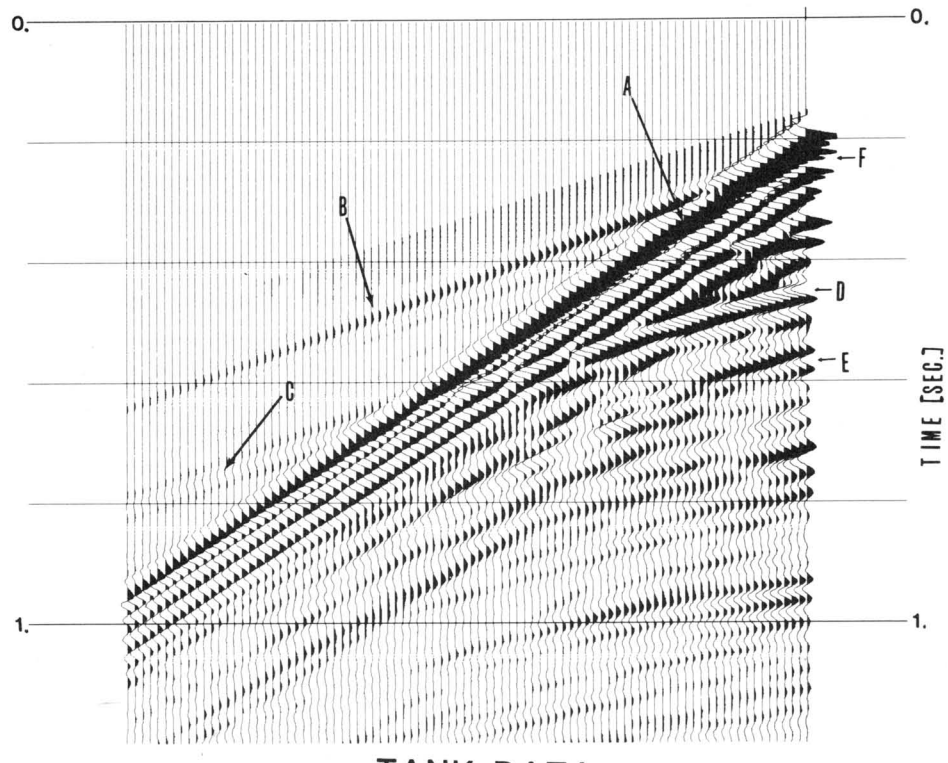

(b)

FIG. 8. (a) Synthetic time section of the physical model. (b) Time section of the physical model.

side boundaries used in this example (see Cerjan et al., 1985). In the *S*-wave snapshot (Figure 4b) we see a reflected *S*-wave D, diffractions around the corners A, and a head wave which connects the reflected *S*-wave with the transmitted *P*-wave B (a major part of this event is in the absorbing region), and some noise near the upper right corner C due to the inner reflections near the corner.

The important lesson learned from these examples is that elastic wave propagation presents complicated phenomena even in simple structures. Thus, isolation of *P*- and *S*-waves becomes crucial in the interpretation of events. Since snapshots and time sections show a large number of wavefronts, it is important to calculate their relative amplitudes in order to decide which events can be justifiably ignored.

EXAMPLE: SYNTHETIC SEISMOGRAMS

Next we test the ability of the numerical scheme to produce precise synthetic seismograms for a model which involves strong converted shear phases. Two examples presented are both models consisting of a water layer overlying a stratified solid medium. The first example is a calculated split-spread section and the second is a comparison between numerical results and physical model data.

A split-spread section

A split-spread section was calculated over a three-layer structure consisting of water ($V_p = 1\ 500$ m/s; $V_s = 0$ m/s), upper solid ($V_p = 2\ 700$ m/s, $V_s = 1\ 500$ m/s), and a solid half-space ($V_p = 4\ 000$ m/s; $V_s = 2\ 200$ m/s). The shot-hydrophone configuration and the major raypaths are shown in Figure 5, where capital letters indicate waves traveling in the water and small letters indicate waves traveling in the upper solid. The numerical model used a 256×256 grid with a spacing of $DX = DY = 20$ m. The source (shown by a star in Figure 5) was located in the water and had a Gaussian time dependence with a high-cut frequency of 35 Hz.

Figure 6 shows the calculated time section for this model. The direct *P*-wave A was muted for easier identification of the other events. In Figure 6, event B is the reflection from the water bottom (*PP*-wave), the *PPPP*-wave is indicated by *E*, the two head waves are shown by C from the water bottom, and D from the solid interface. The converted phases are also shown; *PPSP-PSPP* are indicated by F because they both arrive at the same time and the *PSSP*-wave (event G) which arrives later. Note in Figure 6 that both the converted phases show significant amplitudes in the large-offset region.

Comparison with physical tank data

A comparison between a synthetic time section and a time section collected in the acoustic tank of the Seismic Acoustics Laboratory at the University of Houston is presented.

The model size, the shot-hydrophones configuration, and the elastic wave velocities are shown in Figure 7. Figures 8a and 8b show the calculated and tank model time sections, respectively. The differences between the two sections can be attributed to the different types of wavelets used, e.g., the tank data contain a ringy minimum-phase wavelet and appear noisy, while the numerical modeling used a zero-phase wavelet which causes a delay of about 45 ms in the arrival times of the peaks in the synthetic section. In spite of these differences, there is much similarity between the two time sections. For example, the sections include the direct *P*-wave A, the water bottom reflection F, the strong refraction from the water bottom B, the converted phases *PSPP-PPSP* D and their continuation C, and the converted *PSSP* phase E. With more careful study, and by taking into account the wavelet's differences, more events can be successfully compared.

CONCLUSIONS

We presented applications of the elastic Fourier modeling scheme to two important types of geophysical problems, namely, wave propagation in regions containing both vertical and horizontal material heterogeneities, and wave propagation across fluid-solid boundaries. Both problems exhibit strong converted phases which reemphasize that ignoring shear wave energy is often not justified. In practice, remnants of the converted phases are present even after common-depth-point stacking in a manner similar to the presence of multiples on these sections. Because elastic wave propagation is more complicated than acoustic propagation, elastic forward modeling gains additional importance in deciphering events. This study shows that many phases appear on the time sections and snapshots, and therefore it is important to have an accurate amplitude evaluation for determining the relative importance of each event.

The Fourier method, with its accurate spatial derivative approximation, proved adequate for forward modeling of typical 2-D geophysical problems. By taking the numerical divergence and curl, the method isolated *P*-waves from *S*-waves, and thus facilitated the interpretation. The method also handled the mathematicaly complicated problem of wave propagation in a region containing fluids and solids in planar contact. Comparison with physical modeling data for this case proved satisfactory to within the differences expected as a result of the different source wavelets and source types in the two examples. However, for nonhorizontal fluid-solid contacts, we found that the method generates noise from diffractions from the grid points along the interface, and further work is required to remedy this problem.

REFERENCES

Cerjan, C., Kosloff, D., Kosloff, R., and Reshef, M., 1985, A nonreflecting boundary condition for discrete acoustic and elastic wave calculation: Geophysics, **50**, 705–708.

Kosloff, D., Reshef, M., and Loewenthal, D., 1984, Elastic wave calculations by the Fourier method: Bull., Seism. Soc. Am., **74**, 875–891.